

University of Wollongong

Research Online

Australian Institute for Innovative Materials -
Papers

Australian Institute for Innovative Materials

2017

Atomic Interface Engineering and Electric-Field Effect in Ultrathin Bi₂MoO₆ Nanosheets for Superior Lithium Ion Storage

Yang Zheng

University of Wollongong, yz966@uowmail.edu.au

Tengfei Zhou

University of Wollongong, tz765@uowmail.edu.au

Xudong Zhao

Tianjin University

Wei Kong Pang

University of Wollongong, wkpang@uow.edu.au

Hong Gao

University of Wollongong, hg173@uowmail.edu.au

See next page for additional authors

Follow this and additional works at: <https://ro.uow.edu.au/aiimpapers>



Part of the [Engineering Commons](#), and the [Physical Sciences and Mathematics Commons](#)

Recommended Citation

Zheng, Yang; Zhou, Tengfei; Zhao, Xudong; Pang, Wei Kong; Gao, Hong; Li, Sean; Zhou, Zhen; Liu, Hua-Kun; and Guo, Zaiping, "Atomic Interface Engineering and Electric-Field Effect in Ultrathin Bi₂MoO₆ Nanosheets for Superior Lithium Ion Storage" (2017). *Australian Institute for Innovative Materials - Papers*. 2515.
<https://ro.uow.edu.au/aiimpapers/2515>

Research Online is the open access institutional repository for the University of Wollongong. For further information contact the UOW Library: research-pubs@uow.edu.au

Atomic Interface Engineering and Electric-Field Effect in Ultrathin Bi₂MoO₆ Nanosheets for Superior Lithium Ion Storage

Abstract

Ultrathin 2D materials can offer promising opportunities for exploring advanced energy storage systems, with satisfactory electrochemical performance. Engineering atomic interfaces by stacking 2D crystals holds huge potential for tuning material properties at the atomic level, owing to the strong layer-layer interactions, enabling unprecedented physical properties. In this work, atomically thin Bi₂MoO₆ sheets are acquired that exhibit remarkable high-rate cycling performance in Li-ion batteries, which can be ascribed to the interlayer coupling effect, as well as the 2D configuration and intrinsic structural stability. The unbalanced charge distribution occurs within the crystal and induces built-in electric fields, significantly boosting lithium ion transfer dynamics, while the extra charge transport channels generated on the open surfaces further promote charge transport. The in situ synchrotron X-ray powder diffraction results confirm the material's excellent structural stability. This work provides some insights for designing high-performance electrode materials for energy storage by manipulating the interface interaction and electronic structure.

Disciplines

Engineering | Physical Sciences and Mathematics

Publication Details

Zheng, Y., Zhou, T., Zhao, X., Pang, W. Kong., Gao, H., Li, S., Zhou, Z., Liu, H. & Guo, Z. (2017). Atomic Interface Engineering and Electric-Field Effect in Ultrathin Bi₂MoO₆ Nanosheets for Superior Lithium Ion Storage. *Advanced Materials*, 29 (26), 1700396-1-1700396-8.

Authors

Yang Zheng, Tengfei Zhou, Xudong Zhao, Wei Kong Pang, Hong Gao, Sean Li, Zhen Zhou, Hua-Kun Liu, and Zaiping Guo

DOI: 10.1002/(adma.201700396)

Article type: Communication

Atomic Interface Engineering and Electric-Field Effect in Ultrathin Bi₂MoO₆ Nanosheets for Superior Lithium Ion Storage

*Yang Zheng, Tengfei Zhou, Xudong Zhao, Wei Kong Pang, Hong Gao, Sean Li, Zhen Zhou, Huakun Liu, and Zaiping Guo**

Y. Zheng, Dr. T. Zhou, Dr. W. K. Pang, H. Gao, Prof. H. Liu, Prof. Z. Guo
Institute for Superconducting & Electronic Materials, School of Mechanical, Materials and Mechatronics Engineering, University of Wollongong, Wollongong, NSW 2522, Australia
E-mail: zguo@uow.edu.au

X. Zhao, Prof. Z. Zhou
Institute of New Energy Material Chemistry, School of Materials Science and Engineering, Nankai University, Tianjin 300071, China

Prof. S. Li
School of Materials Science and Engineering, University of New South Wales, NSW 2052, Australia

Keywords: Bi₂MoO₆, atomic interface, electric field, ultrathin sheet, lithium-ion battery

Abstract: Ultrathin two-dimensional (2D) materials can offer promising opportunities for exploring advanced energy storage systems with satisfactory electrochemical performance. Engineering atomic interfaces by stacking 2D crystals holds huge potential for tuning material properties at the atomic level, owing to the strong layer-layer interactions, enabling unprecedented physics. In this work, atomically-thin Bi₂MoO₆ sheets were acquired and exhibited remarkable high-rate cycling performance in Li-ion batteries, which can be ascribed to the interlayer coupling effect, as well as the 2D configuration and intrinsic structural stability. The unbalanced charge distribution occurs within the crystal and induces built-in electric fields, significantly boosting lithium ion transfer dynamics, while the extra charge transport channels generated on the open surfaces further promote charge transport. The in-situ synchrotron X-ray powder diffraction results confirmed the material's excellent structural stability. This work will provide some insights for designing high-performance electrode materials for energy storage by manipulating the interface interaction and electronic structure.

High performance lithium-ion batteries (LIBs) are currently the most promising energy storage technology to satisfy the ever-growing demands for portable electronics and electrical transportation.^[1-5] Since existing commercial graphite anodes are approaching their limits,^[6] novel electrode materials with excellent high-rate capability and ultra-long lifespan are highly desirable, which is the key step toward enabling LIBs integration into large-scale energy storage systems. It is widely recognized that dimensionality, composition, and atomic arrangement play important roles in determining the intrinsic properties of materials,^[7] markedly influencing their electrochemical activity in energy storage. Therefore, ingenious designs that synergistically optimize these characteristics may allow for the creation of electrodes with the desired properties, which is desperately needed, although significant challenges still remain to date.

Ultrathin two-dimensional (2D) materials hold great potential for exploring advanced electrode materials because of their intriguing properties including fast electrochemical reaction, large interlayer space, ultrahigh surface area and tunable electronic properties, leading to improved electrochemical performance for LIBs.^[8-10] In particular, their open surfaces potentially provide additional shortened paths for ionic/electronic transport,^[11,12] while the atomic defects induced by oxygen vacancies or dangling bonds typically trigger unexpected changes in electronic states, consequently affording higher charge mobility.^[13,14] Despite some progress in realizing 2D materials with atomic thickness, current approaches mostly rely on chemical vapor deposition^[15] or mechanical exfoliation^[16] techniques via exfoliating bulk compounds, particularly, liquid exfoliation of van der Waals layered crystals, such as transition metal chalcogenides, phosphorene, and transition metals carbides and carbonitrides.^[17-19] Unfortunately, such poor scalability and complicated processes make it difficult to scale up to a practical level. Furthermore, exfoliating other materials, especially complex oxides stacked with ionically bonded layers, is exceedingly challenging. Nevertheless, it is well established that ternary metal oxides generally show higher

electrochemical activities than binary metal oxides, owing to the complex composition and synergistic effects of multiple metal species.^[20]

Besides the aforementioned factors, the interface interplay among materials could effectively tailor their physicochemical properties as well,^[21,22] considering that the charge/mass transfer process and most chemical reactions are occurring at the interface. More importantly, coupling of 2D materials to create heterogeneous interfaces can further alter their performance in electrochemical applications, since charge redistribution and structural distortion might occur.^[23,24] For example, a 2D MoS₂/C nanosheet superstructure exhibited superior Li storage performance, which was attributed to the ideal atomic interface contact between the monolayer MoS₂ and carbon, contributing to a strong interface synergistic effect.^[25] Ultra-fast charge transfer occurred very efficiently in atomically thin MoS₂/WS₂ heterolayers.^[26] Unlike conventional heterogeneous interfaces constructed by assembling disparate crystals together, the inherent atomic interfaces formed in an individual ultrathin 2D ternary material may possess better electrochemical properties because of the strong chemical bonds and perfect lattice match between neighboring layers, thus tuning the electron distribution and maximizing the interaction at the interface. Of particular note is that sufficient hybridization of atomic orbitals at an interface with strong ionic bonds allows carrier delocalization, which promotes charge transfer across the interface, leading to band bending and the formation of a built-in potential.^[27] Interestingly, recent work has revealed that such a built-in electric field within the heterointerfaces could boost interfacial charge transfer and accelerate reaction kinetics.^[28] Herein, rational construction of well-defined ternary metal oxide nanosheets with atomic thickness might be an effective approach to optimize the electrochemical performance by coupling unique structural features in terms of atomic interface interactions and the electric-field effect.

Here, a facile and scalable wet-chemical synthesis approach has been introduced for fabrication of atomically thin Bi₂MoO₆ nanosheets (BMO sheets), consisting of alternate

stacking of $[\text{Bi}_2\text{O}_2]$ and $[\text{MoO}_4]$ layers, with large interlayer channels. Interestingly, the self-adaptive oxygen vacancies produced on the open surfaces of BMO sheets is explicitly confirmed by X-ray photoelectron spectroscopy (XPS) and electron paramagnetic resonance (EPR) spectra. More intriguingly, the density functional theory (DFT) calculations demonstrate that an unbalanced charge distribution could occur between the stacked layers as well as around the oxygen vacancies, which induces an interfacial electric field within the interface and local in-panel electric field on the open surfaces, thus accelerating Li ion diffusion kinetics and promoting high-rate capability. In addition, extra migration paths formed on the open interfaces would facilitate charge transport, thereby further enhancing the Li storage performance. Benefiting from the unique structure ensured by the coupling effect of the atomic interfaces, the present atomically thin BMO sheets exhibit extraordinary high-rate capability and ultra-long cycling stability, showing enormous potential for next-generation LIB anode. More importantly, this work demonstrates a powerful multi-scale coordinated strategy for designing advanced electrode materials for electrochemical energy storage, including synergistic modulation of the dimensionality, composition, atomic arrangement, and interfaces.

The typical scanning electron microscope (SEM) and transmission electron microscope (TEM) images in Figure 1a,b visually confirm the sheet-like morphology of the obtained ultrathin BMO. Figure 1c shows a representative TEM image, which is a lateral view of the marked nanosheet in Figure 1b and reveals the well-defined layer-like architecture with a thickness of about 2.45 nm, corresponding to 1.5 layers of orthorhombic Bi_2MoO_6 unit cell along the b axis. Meanwhile, the high-resolution TEM (HRTEM) image (Figure 1d) demonstrates that the BMO sheets grow along the $[010]$ direction. The lattice spacings of about 0.275 nm and 0.274 nm respectively correspond to the (002) and (200) planes of orthorhombic Bi_2MoO_6 ,^[29] indicating that the BMO sheets preferentially expose the $\{010\}$ facets. What is interesting is that some structural defects/disorder are generated around the

exposed surface, which might affect the electronic structure of the material, thus, in turn, tailoring its electrochemical properties.^[30] More importantly, the lateral high-angle annular dark-field-scanning transmission electron microscope (HAADF-STEM) imaging further clearly reveals the crystal structure of the BMO sheets (Figure 1e). In principle, the signal intensity in the HAADF image is proportional to the atomic number, while the O atoms are invisible. Hence, the brighter spots stand for Bi atoms, and the spots with lower brightness represent Mo atoms, demonstrating that the arrangement of Bi and Mo atoms in the ultrathin sheets is highly consistent with the schematic diagram of the Bi_2MoO_6 crystal structure (Figure 1f). Elemental mapping (Figure 1g–j) indicates that Bi, Mo, and O coexist and are distributed uniformly in the ultrathin sheets. The acquired BMO sheets have an average sheet thickness of 1.61 nm, as determined by atomic force microscopy (Figure 1k,l), close to the 1.62 nm thickness of a BMO along the [010] direction, which is in good agreement with the TEM results. In addition, the morphologies of the obtained micro-sized BMO (BMO bulk), ultrathin sheets of Bi_2O_3 (BO sheets) and MoO_3 (MO sheets), and their mixture (BO+MO sheets) can be verified by the SEM and TEM results (Figure S1–S5, Supporting Information).

The crystalline nature and purity of the resultant samples were examined by powder X-ray diffraction (XRD). As shown in Figure 2a, all the diffraction peaks of BMO sheets can be readily indexed to the orthorhombic Bi_2MoO_6 (JCPDS No. 77-1246), indicating the highly purity of prepared nanosheets. Compared to the bulk sample, however, only four broadened and weak diffraction peaks emerged, demonstrating the ultrathin thickness and small particle size of the BMO sheets. Interestingly, the intensity ratio $I(060)/I(131)$ of the BMO sheets represents a dramatic enhancement relative to their bulk counterpart, suggesting that the BMO sheets preferentially grow along the [010] direction, which is in agreement with the TEM results (Figure 1d). The structures of the acquired BMO products were characterized by Raman spectroscopy. As can be seen from Figure 2b, well-defined phonon modes were observed in the 200–1000 cm^{-1} wavenumber range, corresponding to the vibrational modes of

orthorhombic Bi_2MoO_6 and confirming the formation of pure Bi_2MoO_6 .^[31] Specifically, the Raman bands at $700\text{--}850\text{ cm}^{-1}$ correspond to the stretching vibrations of MoO_6 octahedra, while the presence of the modes in the $230\text{--}460\text{ cm}^{-1}$ range can be assigned to the bending motions of the MoO_6 octahedra and BiO_3 tetrahedra. It is notable that the Raman peaks of BMO sheets showed broadening and slightly shifted towards lower wave number compared to those of the bulk, further revealing the ultrathin nature of the BMO sheets.^[32] The XRD and Raman results (Figure S6 and S7, Supporting Information) demonstrate the preparation of pure Bi_2O_3 and MoO_3 samples.

The chemical compositions and surface electronic states of the fabricated products were investigated by X-ray photoelectron spectroscopy (XPS). Figure 2c,d displays the high-resolution Bi 4f and O 1s XPS spectra of the BMO products. In contrast to the spectra of the bulk sample, two asymmetric peaks of Bi 4f can be found in the BMO sheets (Figure 2c), signifying the different electronic state of Bi atoms in the ultrathin sheets. Moreover, the deconvoluted shoulder peaks associated with Bi $4f_{5/2}$ (167.3 eV) and Bi $4f_{7/2}$ (161.6 eV) emerge at higher binding energies, revealing that the Bi atoms in the BMO sheets are more electropositive,^[33] due to the rearranged and unsaturated states of the surface Bi and O atoms, resulting in an imbalance in the charge distribution. This would strengthen the interaction between Li ions and electrode materials, and improve the electrochemical activity. In addition, two O 1s peaks located at 529.7 eV and 533.2 eV are observed for both samples, which are attributed to the lattice oxygen and near-surface oxygen, respectively.^[34,35] In particular, a new peak that appeared at 531.7 eV can be assigned to oxygen vacancies.^[34] Furthermore, the Mo 3d peaks of the BMO sheets slightly shifted towards lower binding energy, which is likely due to the bond distortion between the Mo-O atoms in the nanosheets, accompanying with the redistribution of electron density.^[36] The chemical compositions of BO sheets and MO sheets were confirmed by XPS results (Figure S8, Supporting Information). It has been demonstrated that atomic defects, especially oxygen vacancies not only can promote faster charge transport

kinetics, but also help to retain the integrity of the electrode structure, thus enhancing the electrochemical activity.^[14,37] Therefore, it is desirable to introduce oxygen vacancies into the target electrode material to improve its electrochemical performance. Here, electron paramagnetic resonance (EPR) measurements were conducted to offer fingerprint evidence for probing oxygen vacancies.^[35] Figure 2c clearly shows their characteristic EPR signal, revealing the presence of isolated oxygen vacancies in the BMO sheets.

The Li-ion storage behavior of the BMO sheets was initially investigated using cyclic voltammetry (CV). Figure 3a displays representative CV curves for the 1st, 2nd, and 5th cycles at a scan rate of 0.1 mV s⁻¹ in the voltage range of 0.01–2.5 V. The CV curves show multi-peak features, demonstrating that the reaction of the BMO sheets with Li proceeds in multiple steps. During the first negative scan, the cathodic peak at ~1.60 V might be assigned to the insertion of Li-ion into the layered structure of BMO crystal, whereas the small peak at 1.24 V is associated with the reduction of BMO to Bi and Mo metal.^[38,39] An obvious cathodic peak appearing at 0.52 V can be attributed to the formation of the solid electrolyte interphase (SEI) film and the alloying reaction of Bi with Li to form Li₃Bi. Furthermore, the broad reduction peak is divided into two peaks at ~0.74 and 0.61 V in the subsequent cycles, suggesting that the electrochemical lithiation reaction of Bi takes place via two steps (formation of LiBi and Li₃Bi, respectively).^[39] The strong oxidation peak localized at around 0.98 V corresponds to the de-alloying process of Li₃Bi, while the small anodic peaks at about 1.40 V and 1.74 V might be attributed to the oxidation of Mo and Bi, respectively.^[38–40] It is noteworthy that from the second cycle onwards, both the reduction and the oxidation peaks in the CV curves overlap very well, proving that the electrode exhibits good reversibility and stability during the electrochemical reactions. Based on the above analysis, the possible electrochemical reactions of the ultrathin BMO anode are believed to proceed as follows [Reaction (1)–(4)]:



Similarly, the BMO bulk presents CV curves with almost the same shape as those of the BMO sheets, but with poor reversibility during the 1st cycle. The CV curves of the BO+MO sheets show the combination of the redox peaks of the BO sheets and the MO sheets, (Figure S9, Supporting Information).

Galvanostatic discharge/charge measurements were conducted to evaluate the electrochemical performance of the BMO anodes. Remarkably, the BMO sheets achieved a high reversible capacity of 903 mA h g⁻¹ at a current density of 50 mA g⁻¹, with an initial coulombic efficiency (CE) of 78% (Figure 3b,c). In contrast, the BMO bulk exhibited a much lower first-cycle reversible capacity of 770 mA h g⁻¹, corresponding to an initial CE of 70.3% (Figure 3c,d), while the BO+MO sheets showed a CE of 74%, with a specific capacity of 810 mA h g⁻¹. As expected, the BMO sheets or BO+MO sheets showed higher specific capacity and coulombic efficiency compared to the BMO bulk, due to their 2D ultrathin structures, which can provide more transport paths to give access to ions and electrons, accompanied by enhanced energetics for ionic/electronic transfer kinetics. On the other hand, the BMO sheets demonstrate better performance in Li⁺ storage than the BO+MO sheets, which should be attributed to the effects of interlayer coupling in the ultrathin BMO. Importantly, the specific capacity of the BMO sheets was stabilized at 832 mA h g⁻¹ after 80 cycles, (~ 92% capacity retention), manifesting its superior cycling stability.

In addition, the BMO sheets exhibited remarkable rate capability at varied current rates. As shown in Figure 3d, the BMO sheets delivered a reversible capacity of 580 mA h g⁻¹ at a current density of 1000 mA g⁻¹. Even when cycled at a high current density of 2000 mA g⁻¹, a specific capacity of 490 mA h g⁻¹ could be attained, which is higher than for the BMO bulk

and BO+MO sheets. It is well known that long-term cycling stability, especially for charging/discharging at high rate is an important performance for practical application of high-energy LIBs. To further evaluate the high-rate cycling performance, the BMO sheet anode was subjected to prolonged cycling at 1000 mA g^{-1} and 2000 mA g^{-1} , respectively (Figure S10, Supporting Information and Figure 3e). The BMO sheets attained an initial charge capacity of 673 mA h g^{-1} at 1000 mA g^{-1} and retained a large charge capacity of 587 mA h g^{-1} after 1000 cycles, which is much higher than the corresponding values for the bulk BMO, BO sheets, MO sheets, and BO+MO sheets (Figure S11–14, Supporting Information), demonstrating the superior high-rate cycling stability. Encouragingly, even after 1500 cycles at 2000 mA g^{-1} , a high reversible capacity of 478 mA h g^{-1} was still obtainable with an average coulombic efficiency approaching 100% (Figure 3e), suggesting the great promise of 2D BMO for next-generation high-power LIBs. The significantly enhanced high-rate capacity accompanied by exceptional cycling performance for Li storage should be closely related to the unique structure of the BMO sheets. More importantly, the high-rate cycling performance of the present BMO sheets is significantly superior to those of most reported mixed-metal-oxide-based anodes for Li-ion batteries (Table S1, Supporting Information).

To study the structural superiority of BMO material, in-situ synchrotron X-ray powder diffraction (SXRPD) was utilized to reveal the structural changes in the electrode material during the charge/discharge cycling. The variations of the (131), (200)/(002), and (060) reflections were extracted using the single-peak fitting approach, with these being correlated to lattice parameters *a*, *b*, and *c*. The single-peak fitting results suggest that the positions of the (131), (200)/(002), and (060) reflections did not move significantly during the cycling process (Figure S15 and S16, Supporting Information), indicating that the lattice parameters remained nearly unchanged during the electrochemical reactions. The results revealed that the distorted edge-sharing MoO_6 octahedral network and the trigonal-bi-planar BiO_3 are strongly bonded, offering excellent structural stability against the lithiation and delithiation processes, which

explains the outstanding prolonged cycling performance of the Bi_2MoO_6 when used as anode in LIBs. On the other hand, one can also see that the intensities of these reflections are gradually dropping as cycling progresses, despite the charging and discharging, suggesting that pulverization occurs during cycling, as a result of the conversion reaction.

In order to deeply understand the properties of the crystal structure that are responsible for the enhanced lithium storage performance, DFT calculations were performed to investigate the migration barriers to Li^+ along different paths in the BMO bulk and nanosheets. In bulk BMO, three typical lithium diffusion paths were considered (Figure 4a), and the migration paths between the three kinds of binding sites and the corresponding barriers are shown in Figure 4b. Among them, “A” and “B” site are equivalent symmetrically and arranged along the b-axis, while “C” site is in the middle of MoO_4 layer. Along the c-axis in bulk BMO, the crystal can form natural transmission channels with large interlayer spaces between the $[\text{MoO}_4]$ and $[\text{Bi}_2\text{O}_2]$ layers, making them very suitable for Li ion migration. As a result, the barrier from the A to the B sites is only 0.40 eV, whereas the barriers from A and B to C are 1.14 eV and 1.24 eV, respectively, which indicates that Li ions mainly diffuse through the interlayer channels along the c-axis in bulk BMO. For the BMO sheets, the following four kinds of intercalation sites are considered: on the surface O atoms above Bi and Mo, denoted as “A1(B1)” and “A2(B2)”, respectively, and in the interior of the sheets, denoted as “A3(B3)” and “A4(B4)”. It should be noted that, although the transmission channels are distorted to some extent, the BMO sheets show similar or even lower migration barriers of 0.44 and 0.35 eV in these interlayer channels. More importantly, compared to the BMO bulk, the barriers to the migration of Li ions between different binding sites are quite low. As can be seen from Figure 4e, the barrier from the A1 to the A2 site is only 0.76 eV, which is much lower than in BMO bulk (1.14 eV or 1.24 eV). Thus, in the BMO sheets, Li ions could be transferred along both the ab-plane and the c-axis, thereby forming interconnected migration paths on the open surfaces, which is superior to the unidirectional migration in bulk BMO. In

addition, the interlayer electron-electron coupling in the atomically thin BMO was further analyzed (Figure 4f–h). The calculated results signified that the imbalance in the charge distribution occurred between the $[\text{MoO}_4]$ and $[\text{Bi}_2\text{O}_2]$ layers, which could induce a built-in electric field within the atomic interface, thus boosting the Li ion diffusion kinetics and improving the high-rate performance. Furthermore, the charge density distribution around the oxygen vacancies area is calculated theoretically by first principles. As expected, charge redistribution can be observed in the BMO with O-vacancies and an imbalance in charge distribution occurs (Figure S17, Supporting Information), which might induce the formation of a local electric field in plane, contributing to faster charge transfer kinetics.

By combining the in-situ synchrotron XRPD and DFT analysis, a possible mechanism for the enhancement of lithium storage in the atomically thin BMO nanosheets could be proposed (Scheme 1). The unbalanced charge distribution between $[\text{Bi}_2\text{O}_2]^{2+}$ and $[\text{MoO}_4]^{2-}$ layers induces an interfacial electric-field within the interfaces, while lopsided charge distribution around oxygen vacancies resulted in a local in-plane electric-field, thus promoting ion diffusion/electron transport, which can be confirmed by the much lower charge-transfer impedance (Figure S18, Supporting Information) and the high-rate performance (Figure 3d). Meanwhile, benefiting from the structural advantages of the 2D ultrathin construction, interconnected charge migration paths were formed on the open surfaces, which could facilitate the charge transfer process in the BMO sheets, as evidenced by the higher diffusion coefficient of Li^+ (Figure S19, Supporting Information). Therefore, profiting from the strong interlayer coupling effect and atomic defects, which induces built-in electric-field within the crystal and promotes charge transfer dynamics, the superior configuration of the ultrathin sheets, resulting in additional transport paths, as well as the good structural stability ensured by the edge-sharing MoO_6 octahedral network and the trigonal-bi-planar BiO_3 architecture, the BMO sheets exhibit remarkable high-rate capability and outstanding cycling stability for Li-ion storage.

In summary, by means of synergistically modulating their structural configuration and electronic interactions, the atomically-thin BMO nanosheets acquired through a facile wet-chemical synthesis procedure achieved outstanding high-rate cycling performance towards Li-ion batteries. By a combined approach involving DFT calculations and in-situ synchrotron XRPD analysis, the mechanism for the enhancement of lithium storage was investigated in depth. The excellent electrochemical performance can be attributed to the strong electric-field effect within the crystal, the unique 2D ultrathin configuration, and the superior structural stability. The extraordinary high-rate cycling performance, along with the simple and scalable synthetic approach for ultrathin 2D materials, makes this material design strategy a promising approach to exploit novel 2D materials with remarkable performance in advanced energy technologies.

Figure captions:

Figure 1. Morphology of obtained BMO sheets. a) FESEM image. b) TEM image. c) Enlarged high resolution TEM image. In c, the red line marks the thickness of 2.45 nm, corresponding to 1.5 layers of orthorhombic Bi_2MoO_6 unit cell along the b axis. d) HRTEM image. In d, the lattice spacings of 0.274 nm and 0.275 nm are shown, with a dihedral angle of 90° , indicating the {010} exposed lattice plane of BMO sheets. e) Lateral HAADF-STEM image. f) Schematic diagram of orthorhombic Bi_2MoO_6 crystal structure. g–j) Corresponding EDS elemental mappings. k,i) Atomic force microscope (AFM) image and corresponding height profiles.

Figure 2. Structural and compositional characterization of the BMO sheets and bulk sample. a) XRD patterns. b) Raman spectra. c–e) Corresponding high-resolution XPS spectra of Bi 4f, O 1s, and Mo 3d. f) EPR spectra. In d, the new peak at 531.7 eV can be attributed to oxygen vacancies generated on the surface of the BMO sheets. In f, a clear oxygen vacancy signal could be observed in the EPR spectrum of the BMO sheets, indicating the existence of oxygen vacancies in the BMO sheets.

Figure 3. Electrochemical performance of various electrodes for Li storage. a) Cyclic voltammograms for the 1st, 2nd, and 5th cycles of the BMO sheets at a scanning rate of 0.1 mV s⁻¹. b) Galvanostatic discharge-charge profiles for selected cycles of the BMO sheets at 50 mA g⁻¹. c) Cycling performance of BMO sheets, BMO bulk, and BO+MO sheets at 50 mA g⁻¹. d) Rate capabilities of BMO sheets, BMO bulk, and BO+MO sheets at various current densities. e) Long-term cycling performance of the BMO sheets at 2000 mA g⁻¹ and the corresponding coulombic efficiency.

Figure 4. Crystal structure, Li^+ diffusion paths, corresponding migration energy barriers, and charge density distribution calculated by DFT. a) Crystal structure of BMO bulk with three Li ions intercalated at A, B, and C sites. b) Calculated migration energy barriers to Li^+ diffusion through different paths in BMO bulk. c,d) Crystal structure of BMO sheets and four kinds of

intercalation sites. e) Migration energy barriers to Li^+ diffusion along different paths in BMO sheets. f) Crystal structure of the BMO viewed along the [001] direction. g) Charge density distribution of the BMO in the initial state. h) Charge density distribution of the BMO in the charged state ($\text{Li}_2\text{Bi}_2\text{MoO}_6$). In g, the calculated result indicates that the charges are mainly concentrated in the $[\text{MoO}_4]$ layer. Meanwhile, the results based on Bader charge analysis show that the $[\text{MoO}_4]$ and $[\text{Bi}_2\text{O}_2]$ layers are charged at -2.89 e and +2.89 e, respectively. In h, it shown that the imbalance in the charge distribution occurs during the charging state, indicating the presence of the built-in electric field.

Scheme 1. Summary of the enhanced high-rate capacity mechanism of the BMO sheets for LIB. a) The schematic diagram of the induced in-panel electric field and the interface electric field within the BMO sheets viewed along different directions. b) The electric field distribution and the corresponding crystal structure of the BMO sheets in a. c) The relationship between the electric field, migration paths and the Li transfer kinetic in BMO sheets and BMO bulk.

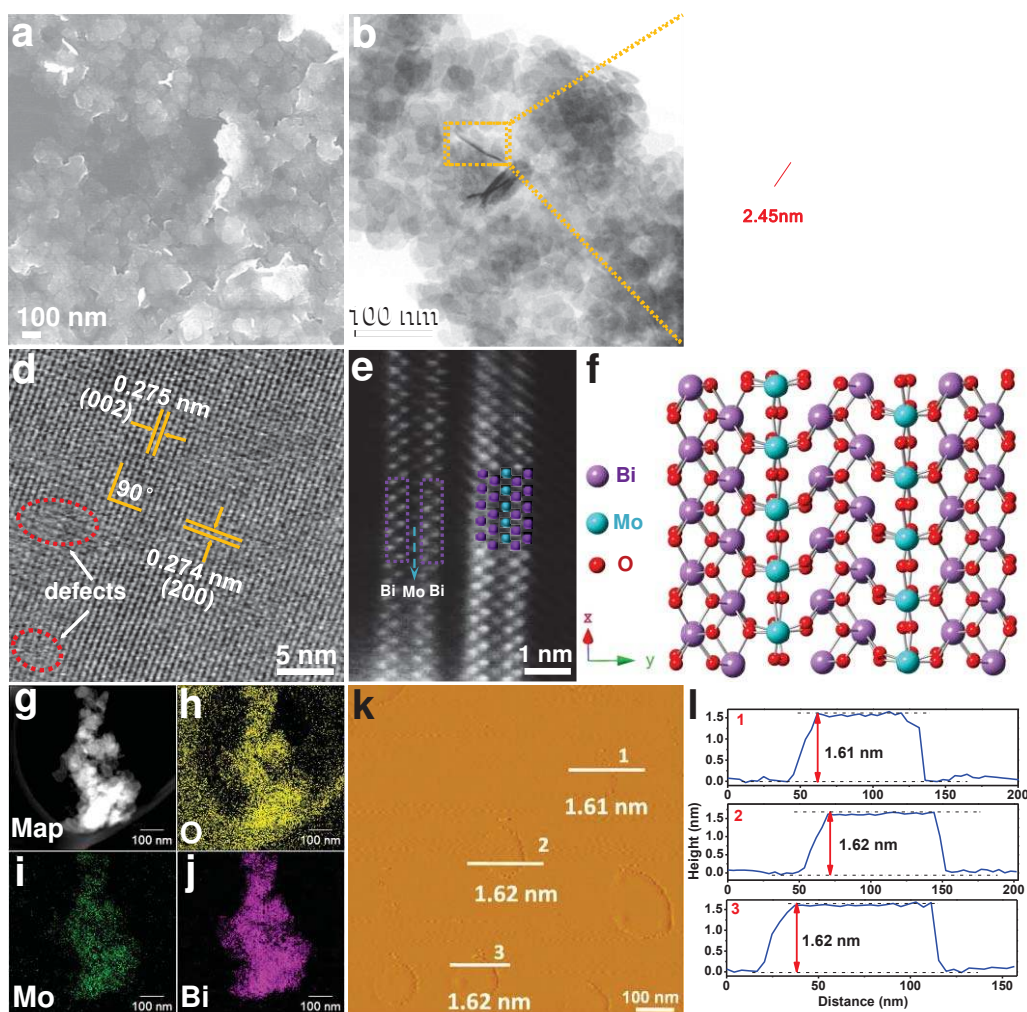


Figure 1. Morphology of obtained BMO sheets. a) FESEM image. b) TEM image. c) Enlarged high resolution TEM image. In c, the red line marks the thickness of 2.45 nm, corresponding to 1.5 layers of orthorhombic Bi_2MoO_6 unit cell along the b axis. d) HRTEM image. In d, the lattice spacings of 0.274 nm and 0.275 nm are shown, with a dihedral angle of 90° , indicating the $\{010\}$ exposed lattice plane of BMO sheets. e) Lateral HAADF-STEM image. f) Schematic diagram of orthorhombic Bi_2MoO_6 crystal structure. g–j) Corresponding EDS elemental mappings. k,i) Atomic force microscope (AFM) image and corresponding height profiles.

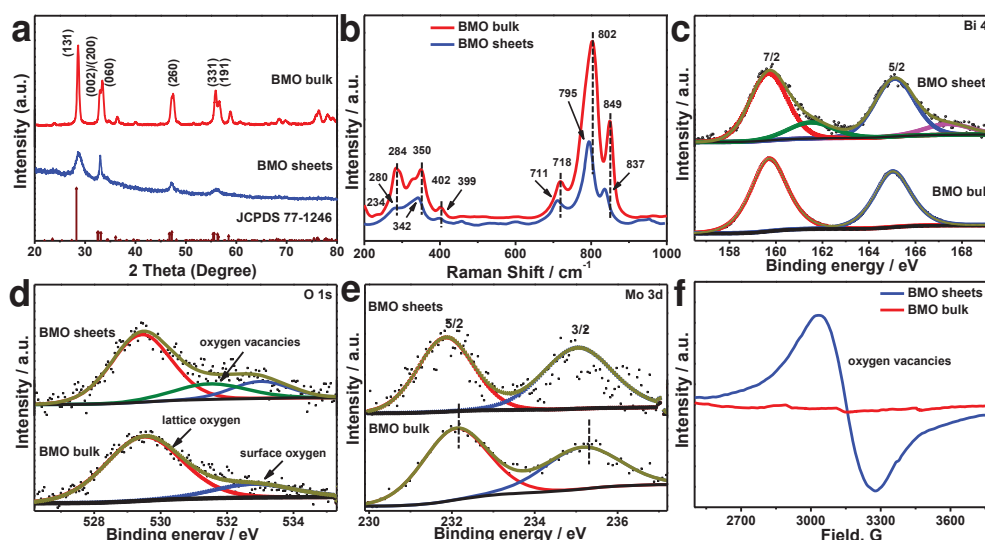


Figure 2. Structural and compositional characterization of the BMO sheets and bulk sample.

a) XRD patterns. b) Raman spectra. c–e) Corresponding high-resolution XPS spectra of Bi 4f, O 1s, and Mo 3d. f) EPR spectra. In d, the new peak at 531.7 eV can be attributed to oxygen vacancies generated on the surface of the BMO sheets. In f, a clear oxygen vacancy signal could be observed in the EPR spectrum of the BMO sheets, indicating the existence of oxygen vacancies in the BMO sheets.

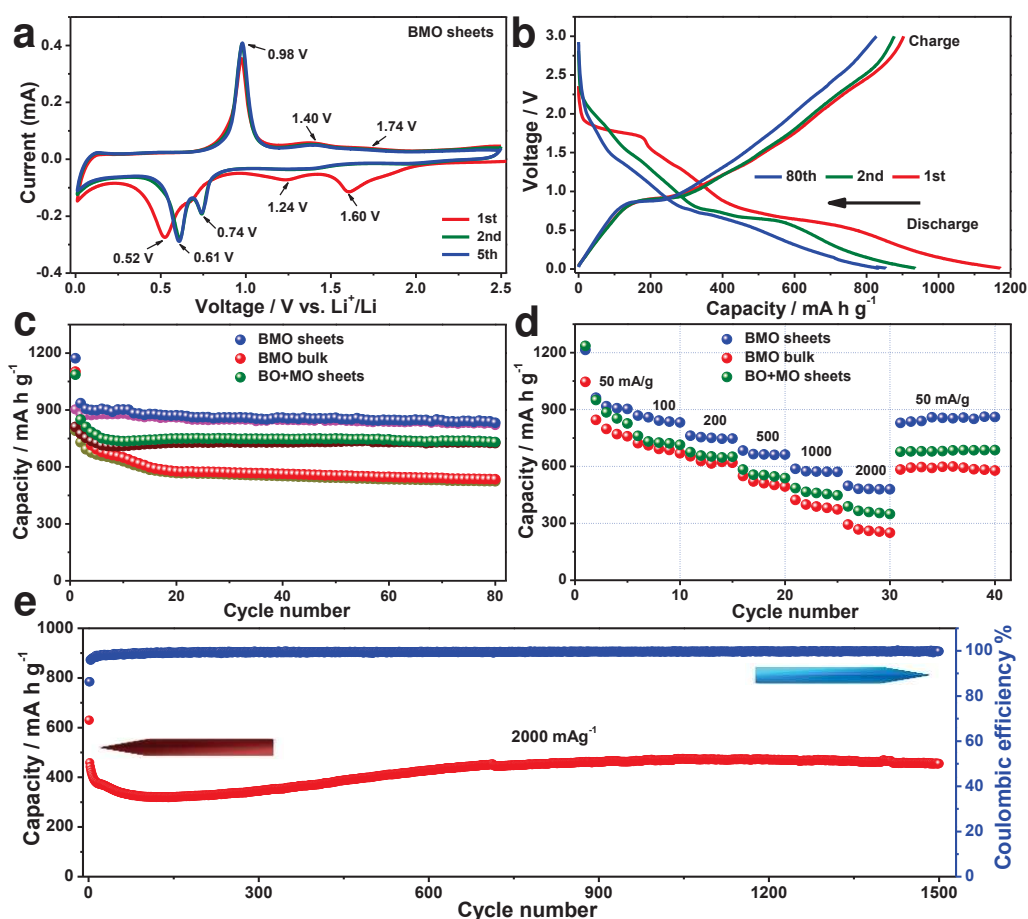


Figure 3. Electrochemical performance of various electrodes for Li storage. a) Cyclic voltammograms for the 1st, 2nd, and 5th cycles of the BMO sheets at a scanning rate of 0.1 mV s⁻¹. b) Galvanostatic discharge-charge profiles for selected cycles of the BMO sheets at 50 mA g⁻¹. c) Cycling performance of BMO sheets, BMO bulk, and BO+MO sheets at 50 mA g⁻¹. d) Rate capabilities of BMO sheets, BMO bulk, and BO+MO sheets at various current densities. e) Long-term cycling performance of the BMO sheets at 2000 mA g⁻¹ and the corresponding coulombic efficiency.

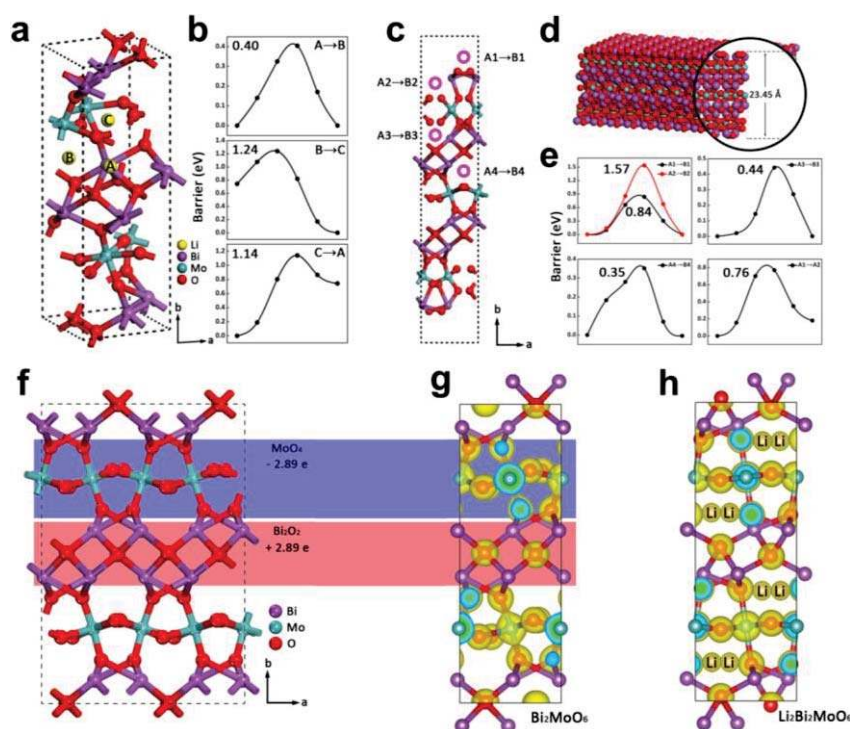
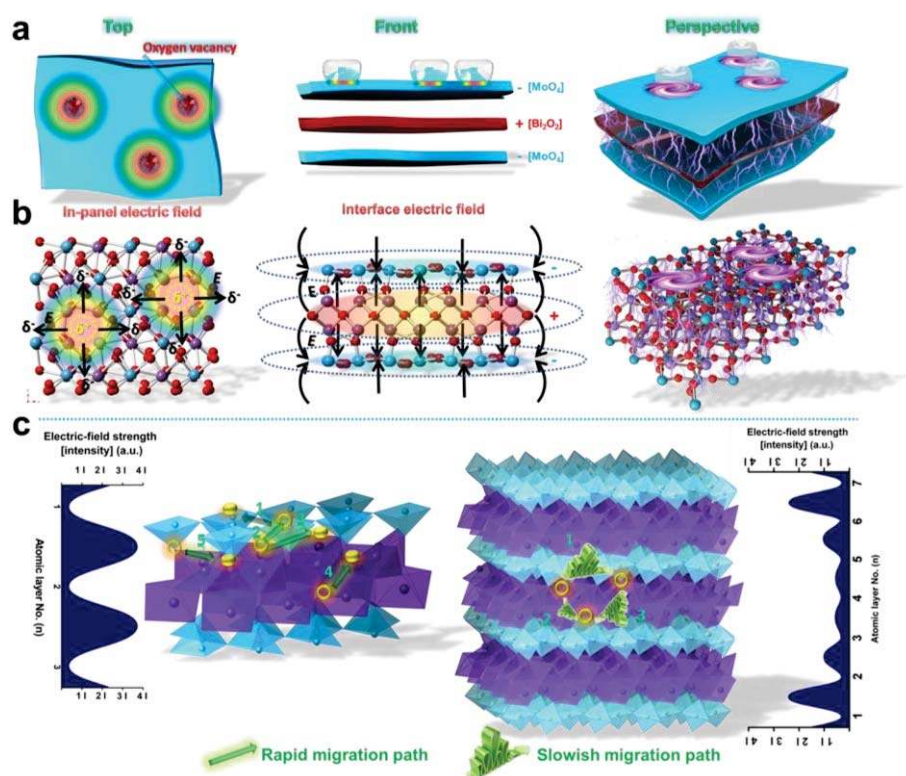


Figure 4. Crystal structure, Li⁺ diffusion paths, corresponding migration energy barriers, and charge density distribution calculated by DFT. a) Crystal structure of BMO bulk with three Li ions intercalated at A, B, and C sites. b) Calculated migration energy barriers to Li⁺ diffusion through different paths in BMO bulk. c,d) Crystal structure of BMO sheets and four kinds of intercalation sites. e) Migration energy barriers to Li⁺ diffusion along different paths in BMO sheets. f) Crystal structure of the BMO viewed along the [001] direction. g) Charge density distribution of the BMO in the initial state. h) Charge density distribution of the BMO in the charged state (Li₂Bi₂MoO₆). In g, the calculated result indicates that the charges are mainly concentrated in the [MoO₄] layer. Meanwhile, the results based on Bader charge analysis show that the [MoO₄] and [Bi₂O₂] layers are charged at -2.89 e and +2.89 e, respectively. In h, it shown that the imbalance in the charge distribution occurs during the charging state, indicating the presence of the built-in electric field.



Scheme 1. Summary of the enhanced high-rate capacity mechanism of the BMO sheets for LIB. a) The schematic diagram of the induced in-panel electric field and the interface electric field within the BMO sheets viewed along different directions. b) The electric field distribution and the corresponding crystal structure of the BMO sheets in a. c) The relationship between the electric field, migration paths and the Li transfer kinetic in BMO sheets and BMO bulk.

Supporting Information

Supporting Information is available from the Wiley Online Library or from the author.

Acknowledgements

Financial support provided by the Australian Research Council (ARC) (FT150100109, FT160100251 and DP170102406) is gratefully acknowledged. We thank the Electron Microscopy Centre (EMC) at the University of Wollongong. We also thank Dr. T. Silver for critical reading of the manuscript. Part of this research was undertaken on the Powder Diffraction beamline at the Australian Synchrotron, Victoria, Australia, and we are grateful for the operational support of Dr. Justin Kimpton. Yang Zheng and Tengfei Zhou contributed equally to this work.

Received: ((will be filled in by the editorial staff))

Revised: ((will be filled in by the editorial staff))

Published online: ((will be filled in by the editorial staff))

References

- [1] M. Armand, J. M. Tarascon, *Nature* **2008**, *451*, 652–657.
- [2] Y. Sun, N. Liu, Y. Cui, *Nature Energy* **2016**, *1*, 16071.
- [3] C. Wu, J. Maier, Y. Yu, *Adv. Mater.* **2016**, *28*, 174–180.
- [4] Q. Xu, J. Y. Li, J. K. Sun, Y. X. Yin, L. J. Wan, Y. G. Guo, *Adv. Energy Mater.* **2017**, *7*, 1601481.
- [5] W. Luo, D. Shen, R. Zhang, B. Zhang, Y. Wang, S. Dou, H. Liu, J. Yang, *Adv. Funct. Mater.* **2016**, *26*, 7800–7806.
- [6] M. Ko, S. Chae, J. Ma, N. Kimet, H.-W. Lee, Y. Cui, J. Cho, *Nature Energy* **2016**, *1*, 16113.
- [7] M. Chhowalla, H. S. Shin, G. Eda, L. J. Li, K. P. Loh, H. Zhang, *Nat. Chem.* **2013**, *5*, 263–275.
- [8] J. Liu, W. Xue, *Adv. Mater.* **2012**, *24*, 4097–4111.
- [9] Y. Jing, Z. Zhou, C. R. Cabrera, Z. Chen, *J. Mater. Chem. A* **2014**, *2*, 12104–12122.
- [10] L. Peng, Y. Zhu, D. Chen, R. S. Ruoff, G. Yu, *Adv. Energy Mater.* **2016**, *6*, 1600025.
- [11] Peng, X. Peng, B. Liu, C. Wu, Y. Xie, G. Yu, *Nano Lett.* **2013**, *13*, 2151–2157.

- [12] Y. Xie, M. Naguib, V. Mochalin, M. Barsoum, Y. Gogotsi, X. Yu, K. Nam, X. Yang, A. Kolesnikov, P. Kent, *J. Am. Chem. Soc.* **2014**, *136*, 6385–6394.
- [13] J. Hong, Z. Hu, M. Probert, K. Li, D. Lv, X. Yang, L. Gu, N. Mao, Q. Feng, L. Xie, J. Zhang, D. Wu, Z. Zhang, C. Jin, W. Li, X. Zhang, J. Yuan, Z. Zhang, *Nat. Commun.* **2015**, *6*, 6293.
- [14] Y. Xu, M. Zhou, X. Wang, C. Wang, L. Liang, F. Grote, M. Wu, Y. Mi, Y. Lei, *Angew. Chem. Int. Ed.* **2015**, *54*, 8768–8771.
- [15] Q. Ji, Y. Zhang, Y. Zhang, Z. Liu, *Chem. Soc. Rev.* **2015**, *44*, 2587–2602.
- [16] H. Li, J. Wu, Z. Yin, H. Zhang, *Acc. Chem. Res.* **2014**, *47*, 1067–1075.
- [17] Q. Zhang, S. Tan, R. Mendes, Z. Sun, Y. Chen, X. Kong, Y. Xue, M. Rümmele, X. Wu, S. Chen, L. Fu, *Adv. Mater.* **2016**, *28*, 2616–2623.
- [18] J. Sun, H. Lee, M. Pasta, H. Yuan, G. Zheng, Y. Sun, Y. Li, Y. Cui, *Nat. Nanotech.* **2015**, *10*, 980–985.
- [19] X. Wang, X. Shen, Y. Gao, Z. Wang, R. Yu, L. Chen, *J. Am. Chem. Soc.* **2015**, *137*, 2715–2721.
- [20] L. Shen, L. Yu, X. Yu, X. Zhang, X. Lou, *Angew. Chem. Int. Ed.* **2015**, *54*, 1868–1872.
- [21] C. Yuan, H. B. Wu, Y. Xie, X. Lou, *Angew. Chem. Int. Ed.* **2014**, *53*, 1488–1504.
- [22] K. X. Wang, X. H. Li, J. S. Chen, *Adv. Mater.* **2015**, *27*, 527–545.
- [23] K. S. Novoselov, A. Mishchenko, A. Carvalho, A. H. Castro Neto, *Science* **2016**, *353*, aac9439.
- [24] B. Peng, G. Yu, X. Liu, B. Liu, X. Liang, L. Bi, K. P. Loh, *2D Mater.* **2016**, *3*, 025020.
- [25] H. Jiang, D. Ren, H. Wang, Y. Hu, S. Guo, H. Yuan, P. Hu, L. Zhang, C. Li, *Adv. Mater.* **2015**, *27*, 3687–3695.
- [26] X. Hong, J. Kim, S. Shi, Y. Zhang, C. Jin, Y. Sun, S. Tongay, J. Wu, Y. Zhang, F. Wang, *Nat. Nanotech.* **2014**, *9*, 682–686.
- [27] D. Jariwala, T. Marks, M. Hersam, *Nat. Mater.* **2017**, *16*, 170–181.

- [28] Y. Zheng, T. Zhou, C. Zhang, J. Mao, H. Liu, Z. Guo, *Angew. Chem. Int. Ed.* **2016**, *55*, 3408–3413.
- [29] T. Zhou, J. Hu, J. Li, *Appl. Catal. B-Environ.* **2011**, *110*, 221–230.
- [30] Y. Sun, S. Gao, F. Lei, Y. Xie, *Chem. Soc. Rev.* **2015**, *44*, 623–636.
- [31] C. Kongmark, R. Coulter, S. Cristol, A. Rubbens, C. Pirovano, A. Löfberg, G. Sankar, W. van Beek, E. Bordes-Richard, R. N. Vannier, *Cryst. Growth Des.* **2012**, *12*, 5994–6003.
- [32] Y. Sun, Z. Sun, S. Gao, H. Cheng, Q. Liu, F. Lei, S. Wei, Y. Xie, *Adv. Energy Mater.* **2014**, *4*, 1300611.
- [33] Y. Zhou, Y. Zhang, M. Lin, J. Long, Z. Zhang, H. Lin, J. C.-S. Wu, X. Wang, *Nat. Commun.* **2015**, *6*, 8340.
- [34] W. Bi, C. Ye, C. Xiao, W. Tong, X. Zhang, W. Shao, Y. Xie, *Small* **2014**, *10*, 2820–2825.
- [35] T. Zhou, Y. Zheng, H. Gao, S. Min, S. Li, H. Liu, Z. Guo, *Adv. Sci.* **2015**, *2*, 1500027.
- [36] Z. Sun, T. Liao, Y. Dou, S. Hwang, M. Park, L. Jiang, J. Kim, S. Dou, *Nat. Commun.* **2014**, *5*, 3813.
- [37] H. Kim, J. Cook, H. Lin, J. Ko, S. Tolbert, V. Ozolins, B. Dunn, *Nat. Mater.* **2017**, *16*, 454–460.
- [38] P. M. Ette, P. Gurunathan, K. Ramesha, *J. Power Sources* **2015**, *278*, 630–638.
- [39] Y. Li, M. Trujillo, E. Fu, B. Patterson, L. Fei, Y. Xu, S. Deng, S. Smirnov, H. Luo, *J. Mater. Chem. A* **2013**, *1*, 12123–12127.
- [40] Z. Wang, S. Madhavi, X. Lou, *J. Phys. Chem. C* **2012**, *116*, 12508–12513.

Atomically-thin Bi_2MoO_6 nanosheets were fabricated and exhibited outstanding high-rate cycling performance towards Li-ion batteries. The excellent electrochemical properties can be ascribed to the strong electric-field effect within the crystal, the unique 2D ultrathin configuration, and the superior structural stability. This work will provide a guide to design novel high-performance electrode materials through the manipulation of interface interaction and electronic structure.

Keyword: Bi_2MoO_6 , atomic interface, electric field, ultrathin sheet, lithium-ion battery

Yang Zheng⁺, Tengfei Zhou⁺, Xudong Zhao, Wei Kong Pang, Hong Gao, Sean Li, Zhen Zhou, Huakun Liu, and Zaiping Guo*

Atomic Interface Engineering and Electric-Field Effect in Ultrathin Bi_2MoO_6 Nanosheets for Superior Lithium Ion Storage

ToC figure (110 mm broad \times 20 mm high)

